RSC Advances

PAPER

View Article Online
View Journal | View Issue

Cite this: *RSC Adv.*, 2025, **15**, 27685

Synergistic effect of porphyrin and NiO in chitosan/graphene oxide aerogels for enhanced photocatalytic degradation of cationic and anionic dyes

Angelos Faraos, [a] Konstantinos N. Maroulas, [a] Emmanouil Nikoloudakis, [b] Charalampos Drivas, [cd] Mark A. Isaacs, [de] George Z. Kyzas [a] and Kalliopi Ladomenou *[a]

The need for clean water has driven the search towards better ways to remove pollutants from wastewater, especially dyes from industrial sources. In this study, we introduce a novel multifunctional aerogel composite CPGNiO(5%)PyP(1%), that brings together five carefully selected components: chitosan, polyvinyl alcohol, graphene oxide, nickel oxide nanoparticles, and a porphyrin-based photosensitizer. By combining these materials, we created a porous, light-responsive system that works exceptionally well under visible light. Using a range of techniques (FT-IR, XRD, SEM/TEM, UV-vis, and XPS), we confirmed the structure and interactions within the hybrid network. When tested against two common dyes, Victoria Blue R (cationic) and Reactive Black 5 (anionic), the composite achieved impressive removal efficiencies of 96.3% and 90.5%, respectively. Further analysis showed that different reactive species (such as holes, hydroxyl, and superoxide radicals) play important roles in the breakdown process. Notably, the material could be reused across multiple cycles without significant loss of performance, and it remained effective even in mixtures of dyes. These results suggest that this composite offers a promising, scalable solution for eco-friendly water purification using visible light, an important step toward more sustainable environmental technologies.

Received 30th June 2025
Accepted 30th July 2025

DOI: 10.1039/d5ra04647e

rsc.li/rsc-advances

1. Introduction

Over the past few decades, rapid industrialization, particularly in the textile, pharmaceutical, printing, and food sectors has led to the widespread use of synthetic dyes, including azo, triphenylmethane, and xanthene derivatives.[1] Although these compounds play a vital role in various manufacturing processes, their discharge into aquatic environments has become a serious environmental issue. Due to their complex aromatic structures and high chemical stability, synthetic dyes are resistant to natural degradation and tend to persist in water bodies.[2] When the dyes are released without adequate treatment, they disrupt aquatic ecosystems and pose health hazards to humans. Prolonged exposure to certain dyes has been associated with skin disorders, carcinogenic effects, and damage to internal organs such as the liver and kidneys. Additionally, their tendency to bioaccumulate in aquatic organisms contributes to food chain disruption and long-term ecological imbalance.[3,4]

Despite the increasing of environmental awareness, the effective removal of dye pollutants from wastewater remains a major challenge.[5] Conventional treatment methods such as biological degradation, adsorption, and electrochemical oxidation, often suffer from significant limitations. Biological processes struggle to break down persistent pollutants, adsorption simply transfers the problem to solid surfaces requiring further treatment, and electrochemical methods can be energy-intensive and may produce harmful by-products.[6–10]

Photocatalysis has emerged as a promising and sustainable alternative method.[11] This light-driven process relies on semiconducting materials to generate reactive species that can break down complex organic pollutants into harmless by-products like carbon dioxide and water.[12] Photocatalysis offers several advantages: it operates under mild conditions, can utilize solar energy, and enables complete mineralization without the need for added chemicals.[13] However, traditional photocatalysts like TiO_2, ZnO, and CdS face significant drawbacks, including poor absorption of visible light, rapid recombination of photoinduced electron–hole pairs, and limited long-term stability.[14–16]

[a]*Hephaestus Laboratory, School of Chemistry, Faculty of Sciences, Democritus University of Thrace, GR-65404 Kavala, Greece. E-mail: kladomenou@chem.duth.gr*

[b]*Institute of Electronic Structure and Laser (IESL), Foundation for Research and Technology – Hellas (FORTH), Heraklion, Greece*

[c]*Department of Chemical Engineering, University of Patras, Patras, 26504, Greece*

[d]*HarwellXPS, Research Complex at Harwell, Rutherford Appleton Labs, OX16 0FA, UK*

[e]*Department of Chemistry, University College London, 20 Gordon Street, London WC1H 0AJ, UK*

To overcome these limitations, recent research has focused on developing advanced photocatalytic materials with enhanced visible-light absorption, improved charge separation, and larger surface areas. Materials such as metal organic frameworks (MOFs), graphitic carbon nitride (g-C_3N_4), and carbon-based nanostructures including graphene, carbon nanotubes, and carbon dots, have shown notable potential.[17–19] In particular, heterojunction and Z-scheme systems have gained attention for their ability to enhance charge carrier separation and improve overall photocatalytic performance under visible light.[20–23] Among these innovative materials, some composites combining biopolymers with nanostructured semiconductors stand out for their environmental friendliness and multifunctionality. One promising example is the ternary composite of chitosan (Cs), polyvinyl alcohol (PVA), and graphene oxide (GO). This combination creates a flexible, hydrophilic matrix rich in functional groups, enhancing dye adsorption and facilitating electron transfer. The incorporation of nickel oxide (NiO), a p-type semiconductor with strong oxidative potential, further enhances photocatalytic activity.[24] For instance, adding just 5 w/w% NiO into Cs/PVA matrices, the methyl orange removal efficiency under visible light becomes more than doubled, while imparting antibacterial properties.[25] To further exploit visible-light photocatalytic activity, researchers have introduced a cationic porphyrin photosensitizer meso-tetra(*N*-methylpyridyl)porphyrin (PyP), onto GO-based composites.[26,27] PyP-GO hybrids exhibit rapid photoinduced electron transfer with efficiencies exceeding 90%, significantly improving dye degradation.[28] Some photocurrent analyses confirm that these systems enhance charge separation and reactive oxygen species (ROS) generation under visible light. Chitosan/GO-based hydrogels have demonstrated remarkable reusability and dye selectivity, effectively removing both cationic (methylene blue, rhodamine B) and anionic (methyl orange, Congo red) dyes over multiple cycles.[25] Furthermore, PyP-immobilized platforms, such as porphyrin–MOF systems, have shown enhanced visible-light absorption and ROS generation toward dyes like methyl orange.[29]

Beyond their photocatalytic potential, Cs-PVA-GO composites have found use in a range of applications, including biomaterials, supercapacitors, and mechanically robust supports.[28,30–33] The inclusion of NiO nanoparticles significantly modifies their functionality, introducing new photocatalytic and antibacterial properties. Meanwhile, PyP has been widely studied for its applications in photocatalysis and hydrogen evolution.[34–37]

Despite the promising results from individual two and three combinations such as Cs–NiO, Cs-porphyrin, Cs-GO, GO–NiO, and GO-porphyrin, there remains a lack of studies integrating all five components (Cs, PVA, GO, NiO, and PyP) into a single, visible-light-responsive nanocomposite system.[38–45] To address this gap, five composite materials: (i) a reference Cs–PVA–GO (CPG), and four functionalized variants: CPG with 5 w/w % NiO (CPGNiO(5%)); CPGNiO(5%) with 1 w/w% PyP [CPGNiO(5%)PyP(1%)]; CPGNiO(5%) with 0.5 w/w% PyP [CPGNiO(5%)PyP(0.5%)]; and CPG with 10 w/w% NiO and 0.5 w/w% PyP [CPGNiO(10%)PyP(0.5%)] were synthesized and characterized. The influence of varying NiO and PyP concentrations on the photocatalytic activity of the composites under visible-light irradiation was investigated.

As model pollutants, two structurally and functionally distinct dyes were selected; Victoria Blue R (VBR), a mutagenic cationic triphenylmethane dye which is commonly used in cosmetics, and Reactive Black 5 (RB5), which is a persistent anionic azo dye widely employed in textile applications. These dyes were used as representative models to evaluate the selectivity and broad-spectrum applicability of the photocatalysts. The synergistic photocatalytic mechanisms operating within these hybrid composites are elucidated, and their potential for scalable, visible-light-driven water purification applications is highlighted.

2. Materials and methods

2.1. Materials

All materials were used as received. Graphite flakes (75% over 150 μm, 332 461), sulfuric acid (98% w/v), potassium permanganate (ACS reagent, ≥99.0%) and hydrogen peroxide (30% w/w in H_2O) were supplied from Merck Ltd. Chitosan (310–375 kDa, DDA > 75%), poly(vinyl alcohol) (MW 13,000–23,000 g mol^{-1}, 87–89% hydrolysed), sodium tripolyphosphate (TPP, $Na_5O_{10}P_3$) and NiO were purchased from Sigma-Aldrich. Meso-tetra(*N*-methylpyridyl)porphyrin (PyP) was synthesised according to the literature.[46]

2.2. Synthesis of photocatalysts

GO was synthesized based on a previous work.[47] A solution of 1% w/v Cs (solution A) was prepared by dissolving a certain amount of Cs in 2% v/v acetic acid aqueous solution. Then, PVA powder was dissolved into DI water at 80 °C and was stirred for 4 h to obtain 1% PVA solution (solution B). Finally, GO was mixed with DI water, NiO and PyP followed by ultrasonication until a homogeneous solution was obtained (Solution C). The three solutions were mixed and stirred for 3 h and then PyP was added as the crosslinking agent, turning the solution to gel phase. The sol–gel that was formed was put in the freezer for 24 h. It was freeze-dried at −104 °C for 48 h to produce the aerogel. Finally, the aerogel was purified with water/methanol mixture in a Soxhlet apparatus for 24 h, thus obtaining CPGNiOPyP. Similar procedure was followed for the control materials. Table 1 summarizes the catalysts prepared and tested in the current study.

Table 1 Summary of catalysts and the ratio (% w/w) of each material used

Material	Cs	GO	PVA	NiO	PyP
CPG	1	0.01	0.25	—	—
CPGNiO(5%)	1	0.01	0.25	0.05	—
CPGNiO(5%)PyP(0.5%)	1	0.01	0.25	0.05	0.005
CPGNiO(10%)PyP(0.5%)	1	0.01	0.25	0.1	0.005
CPGNiO(5%)PyP(1%)	1	0.01	0.25	0.05	0.01

2.3. Characterization techniques

All materials were analyzed with various characterization techniques. Fourier transform infrared spectroscopy (FT-IR) analysis was used to characterize the functional groups of all the materials. The laboratory utilized the PerkinElmer Frontier attenuated total reflectance Fourier transform infrared spectrometer with a nominal resolution of 2 cm^{-1}. The spectra range of the FT-IR analysis was 4000–550 cm^{-1}. For the UV-vis measurements we used a UV-2600 Shimadzu instrument. Using a BRUKER D8 FOCUS X-ray diffractometer with CuKα radiation (λ = 0.154 nm), crystallinity was detected over a 2θ degree range of 5–90°. To scan the surface and characterize the morphology of the materials, JEOL JSM6390LV scanning electron microscope (SEM) was used. A transmission electron microscopy (TEM) system (Model JEM-2100F electron microscope (JEOL, Japan)) was used for morphology characterization of C-Dots. A dilute stock solution was deposited onto the grid for subsequent HRTEM imaging, using an 80 kV accelerating voltage. Kratos XPS data was acquired using a Kratos Axis SUPRA using monochromated Al kα (1486.69 eV) X-rays at 15 mA emission and 15 kV HT (225 W) and an analysis area of 700 × 400 μm. The instrument was calibrated to gold metal Au 4f (83.95 eV) and dispersion adjusted give a BE of 932.6 eV for the Cu 2p3/2 line of metallic copper. Ag 3d5/2 line FWHM at 10 eV pass energy was 0.54 eV. Source resolution for monochromatic Al Kα X-rays is ~0.3 eV. The instrumental resolution was determined to be 0.29 eV at 10 eV pass energy using the Fermi edge of the valence band for metallic silver. Instrument resolution with charge compensation system on determined to be < 1.33 eV FWHM on PTFE. High resolution spectra of the elements of interest were obtained individually using a pass energy of 40 eV, step size of 0.1 eV and dwell time of 280 ms, resulting in a line width of *ca.* 0.7 eV for Au 4f7/2. The survey spectrum was obtained using a pass energy of 80 eV. Charge neutralization was achieved using an electron flood gun with filament current = 0.4 A, charge balance = 4 V, filament bias = 5 V. Successful neutralization was adjudged by analyzing the C 1s region wherein a sharp peak with no lower BE structure was obtained. Spectra have been charged corrected to lowest BE component of the C 1s spectrum at 284.8 eV, attributed to the C–C/C–H bonds. All data was recorded at a base pressure of below 9 × 10^{-9} Torr and a room temperature of 294 K. The sample was mounted on the stage prior to its introduction into the vacuum chamber by pressing the powder into copper tape. Utilizing a SHIMADZU UV-vis spectrophotometer at λ_{max} = 610 nm, the degradation rate of VBR was estimated by measuring the change in VBR absorption *vs.* irradiation time, by using different materials each time. As a blank sample, deionized water was used.

2.4. Experimental procedure of photocatalytic degradation

An amount of 5 mg of catalyst was dispersed in 10 mL of an aqueous VBR solution (initial concentration of 15 mg L^{-1}) in a test tube and stirred continuously at room temperature (22 °C) in the dark for 30 min to establish adsorption–desorption equilibrium between the catalyst and the dye.[48,49] The photocatalytic activity of the materials that were used, were evaluated under visible irradiation with a 100 W white led emitting lamp, every 30 min for their dye breakdown efficiency. The distance between the test tube and the lamp was fixed at 12 cm. Same experiments were carried out on RB5 dye solution (with initial concentration of 75 mg L^{-1}).[50,51]

In order to elucidate the mechanism of the catalyst, various scavengers were added during the photocatalytic reactions. After dark equilibration, the appropriate scavenger was added to the suspension. All scavengers were added to the dye solution at a fixed concentration of 5 mM. Each scavenger test was performed independently to avoid interference.[52] Following the addition of each scavenger, the suspension was irradiated under visible light and analysed using a UV-vis spectrophotometer by monitoring the absorbance at the maximum wavelength (λ_{max}) of the target dye. Control experiments without scavengers were also conducted under identical conditions to assess the unperturbed photocatalytic activity. The percentage removal R (%) of VBR and RB5 was determined with eqn (1),

$$R(\%) = \frac{C_0 - C_f}{C_0} \times 100\% \quad (1)$$

where C_0 is the initial concentration (mg L^{-1}) and C_f is the final concentration (mg L^{-1}), of each dye. To examine the photocatalytic kinetic parameters for the dye's degradation, a pseudo first-order kinetic model was employed with eqn (2),

$$\ln\left(\frac{C_0}{C_f}\right) = k_1 \times t \quad (2)$$

where k_1 is the pseudo first-order rate constant (min^{-1}) and t is the time (min).[53]

3. Results and discussion

3.1. Physicochemical properties of the materials

3.1.1. FT-IR spectra. FT-IR spectra of the materials were investigated, as shown in Fig. 1(a). CPG exhibits the characteristic peaks of Cs, PVA and GO, which were previously described by our lab.[54,55] In particular, the broad peak at 3500–3000 cm^{-1} corresponds to the intra- and inter-molecular O–H units of all materials, as well as the N–H units of Cs.[56] Furthermore, symmetric and asymmetric C–H groups, carbonyl, amide I and amide II are clearly visible at 2890, 1713, 1650 and 1532 cm^{-1}, respectively.[57] Lastly, the peak at 1035 cm^{-1} is attributed to epoxy units, while the peak at 890 cm^{-1} is caused by the interaction of the saccharide structure of Cs and skeletal vibration of PVA.[32] After the addition of NiO, no new peaks are present but only some shifts in wavenumbers. This is possibly due to the low amount of NiO in the composite and also indicates interaction of intermolecular bonds.[58] With the introduction of PyP, there are again mostly some shifts in the wavenumbers of the characteristic peaks. However, a new peak appears at ~610 cm^{-1}, indicative of Ni–O confirming the presence of NiO in the composites.[59]

3.1.2. X-ray diffraction experiments. The X-ray diffraction patterns of CPG, CPGNiO(5%) and CPGNiO(5%)PyP(1%) are presented in Fig. 1(b). In all cases there is a common peak at

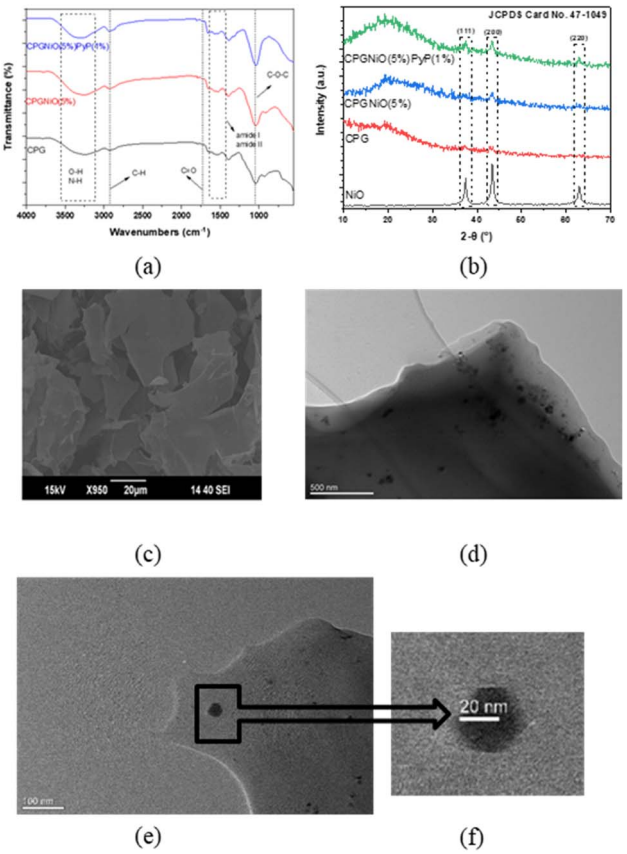

Fig. 1 (a) FT-IR spectra of composites (b) XRD patterns, (c) SEM image, (d–f) TEM images of CPGNiO(5%)PyP(1%).

~20° which can be attributed both to Cs and PVA and is common in the Cs/PVA composites.[60] In the materials containing NiO, the presence of Ni is further confirmed by the characteristic structures of NiO which are (111), (200) and (220). It is also visible that the intensity of the Ni peaks in the two composites is reduced, and the corresponding peaks appear broader, compared to pristine NiO. This can be attributed both to the strong interfacial interactions between CPG and NiO particles, which disrupt the crystalline order of the oxide, well as to the uniform dispersion of NiO particles within the composite structure.[61,62] Furthermore, the addition of PyP resulted in sharper peaks and enlarged peak area, indicating expanded crystalline region. Other studies have reported that porphyrins can orient and stabilize metal oxide crystals, leading to stronger diffraction intensities, or that their interaction with graphene can induce structural changes.[63,64]

3.1.3. SEM and TEM images. The Scanning Electron Microscopy (SEM) image of the CPGNiO(5%)PyP(1%) nanocomposite reveals a layered, wrinkled microstructure with overlapping flakes, consistent with GO sheets integrated within a polymeric matrix (Fig. 1(c)). The morphology indicates a well-dispersed hybrid structure, beneficial for electron transfer and active surface area, enhancement. Compared to analogous systems in the literature[39,65,66] this composite exhibit superior structural integration of photosensitizers and metal oxides, which is expected to synergistically improve its photocatalytic and adsorptive performance.

The morphology of CPGNiO(5%)PyP(1%) was shown in Transmission Electron Microscopy (TEM) images (Fig. 1(d–f)). The representative images reveal a heterogeneous structure with well-dispersed nanoparticles within a continuous polymeric matrix. The graphene oxide (GO) sheets appear as thin, wrinkled, and semi-transparent layers which form the foundational framework of the material.[67] Their large surface area and flexible morphology provide an ideal support for anchoring both nanoparticles and organic molecules. Scattered across these GO sheets are nickel oxide (NiO) nanoparticles, which show up as small, dark, nearly spherical spots.[68]

These particles are well-dispersed and uniform in size typically within the 5–20 nm range, indicating that they have been successfully nucleated and stabilized on the GO surface. His observation parallels findings of ~18 nm cubic NiO particles in PVA-based blends.[69] This even distribution is likely the result of favorable interactions, such as hydrogen bonding and electrostatic forces, between NiO and the functional groups present in both GO and chitosan. Although chitosan and polyvinyl alcohol (PVA) are not directly visible in the images, owing to their low electron contrast, their presence is suggested by a faint, amorphous halo surrounding the GO-NiO structures. This "coating" effect implies that these polymers wrap around or embed the inorganic components, contributing to better stability in solution and improved film-forming capabilities. In some regions, we can also spot faint, globular features with higher electron density, which likely correspond to the TMPyP porphyrin molecules. These tend to localize near the NiO nanoparticles and the GO surface, hinting at strong π–π interactions between the porphyrin rings and GO.[70–72] This close proximity is promising, as it could help enhance charge separation and light absorption, key factors for efficient photocatalysis. Ahamed *et al.* showed that adding graphene oxide and nickel oxide to a chitosan-PVA blend led to a more uniform structure, with nanoparticles dispersed more evenly throughout the material.[69] Overall, the TEM observations confirm that the composite has formed as intended: a well-integrated hybrid structure where the porphyrin and NiO are anchored within a chitosan-PVA polymeric network on GO sheets. This multi-component architecture is expected to promote synergistic effects, particularly in photocatalytic applications, by combining effective charge transport, structural stability, and light-harvesting functionality.

3.1.4. UV-vis diffuse reflectance spectroscopy (DRS). The optical properties of the synthesized materials were investigated using UV-vis diffuse reflectance spectroscopy (DRS) in solid state, employing the $BaSO_4$ as a reflection standard (Fig. 2(a)). The Kubelka–Munk function was applied to convert reflectance data into absorption spectra and estimate the optical band gaps (Fig. 2(b–d)).

Among the tested samples, CPGNiO(5%)PyP(1%) exhibited characteristic absorption peaks attributed to the porphyrin structure, confirming the successful incorporation of PyP. In detail the Soret band at 425 nm along with the four Q-bands at 522, 563, 581 and 646 nm were clearly observed. In contrast, the

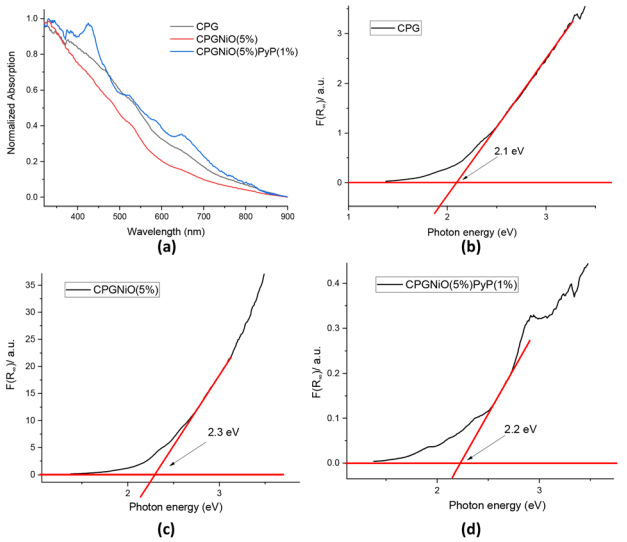

Fig. 2 (a) UV-vis DRS spectra, (b) Tauc plots of CPG, (c) Tauc plots of CPGNiO(5%) and (d) Tauc plots of CPGNiO(5%)PyP(1%).

spectra of CPGNiO(5%) and CPG did not show significant differences, indicating minimal contribution from NiO in terms of distinct absorption features. The estimated band gap energies were 2.2 eV for CPGNiO(5%)PyP(1%), 2.3 eV for CPGNiO(5%), and 2.1 eV for CPG, reflecting slight variations influenced by the composite composition.

These variations, particularly the enhanced visible-light absorption of CPGNiO(5%)PyP(1%) due to porphyrin incorporation, suggest improved potential for photocatalytic activity, which will be discussed in detail in Section 3.

3.1.5. X-ray photoelectron spectroscopy (XPS) analysis. X-ray photoelectron spectroscopy (XPS) was performed to investigate the detailed elemental information of the composites CPGNiO(5%) and CPGNiO(5%)PyP(1%). The survey spectrum, Fig. 3, revealed the presence of C, O, N, P, Na, Ni, and Cl at both samples. For the C 1s region, Fig. 4(a), an asymmetric peak is observed, which upon fitting reveals 4 components at 284.8, 286.3, 287.8, and 288.8 eV attributed to C–C/C–H (61.8%), C–O/C–N (27.9%), C=O (9.2%), and O–C=O (1.1%) respectively.[73] The relative areas for the chemical species are the same, within 10%, for the two samples. One key difference is that the FWHM of the peaks is higher after the addition of the porphyrin, from 1.4 eV to 1.8 eV. This can be explained from the addition of similar carbon species with small variations in binding energies, causing the resulting fitted peaks to appear broader. As will be seen later, the other peaks did not display a change at their FWHM, so charging effect can be ruled out.

The O 1s spectrum, Fig. 4(b), is quite complex because it should contain multiple oxidised carbon species, along with P–O and Na–O bands. Because of that an arbitrary fitting was performed to aid in the understanding of the changes occurring. Only two peaks were used for fitting, and one additional for the Na KLL, one for C=O, $(PO_4)^{3-}$, and Na–O and one more for C=O and $(PO_3)^{-}$.[74] From the fitting it can be seen that upon the porphyrin introduction the lower binding energy peak is increasing compared to the high binding energy one. This means that there is a charge redistribution, the lower the binding energy of the O peak the higher its electron density. For the N 1s region, Fig. 4(c), two peaks can be seen, which after deconvolution appear at 400.1 and 402.6 eV corresponding to N–C (86.5%) and C–N=C (13.5%) respectively.[75] No change is observed between the two samples. The Ni 2p region is presented in Fig. 4(d). At a first glance, it can be seen that the signal for the Ni is about two times more for the sample with the porphyrin. Given that both samples contain the same amount of Ni, we can safely assume that at the one with the porphyrin it is more concentrated at the surface or more exposed. As for its speciation, given the low signal to noise ratio, due to its low

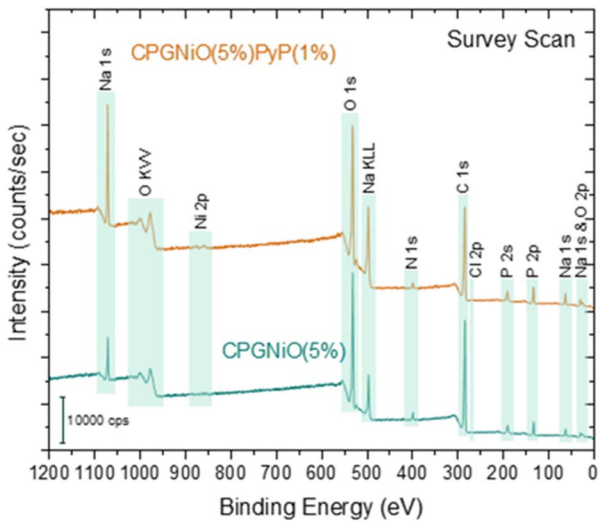

Fig. 3 XPS survey spectra.

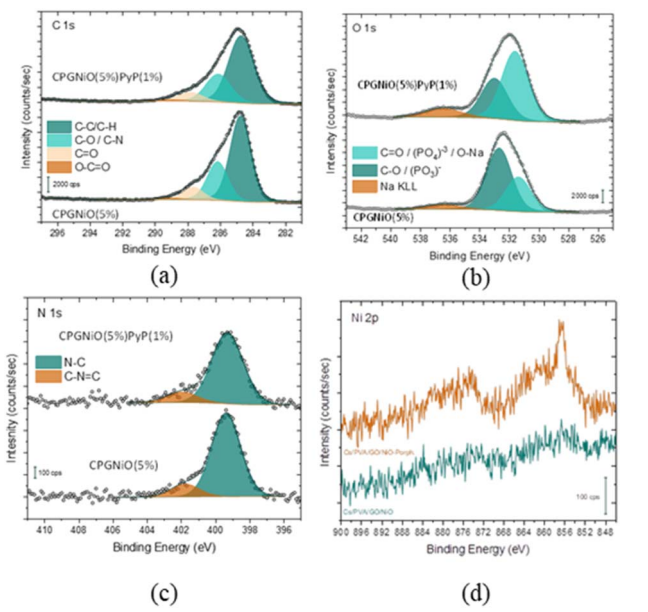

Fig. 4 XPS spectra (a) C 1s, (b) O 1s, (c) N 1s regions, (d) Ni 2p region spectra of CPGNiO(5%) and CPGNiO(5%)PyP(1%).

concentration, a reliable fitting cannot be performed. Judging from the position, 856.5 eV and the shape of the peak, it is, most likely, a mixture of NiO and $Ni(OH)_2$.[76]

Detailed scans of the most prominent peak for each element were collected. Because of the low intensity of some elements the quantification was done using the detailed scans and it shown in Table S1. For the P 2p, Fig. S1a, one peak is observed. Fitting the peak revealed two components, one at 133.5 eV (91.0%) and another small component at 134.9 eV (9.0%) attributed to $(PO_4)^{3-}$ and $(PO_3)^{-}$ respectively.[77] Sodium was present in both samples, possibly due to contamination, as it can be seen in Fig. S1b with the second sample containing 3 time more Na. Additionally, the Cl 2p region was examined to check for contamination. Only traces of Cl were detected, Fig. S1c.

3.2. Efficiency evaluation of the materials

3.2.1 Effect of irradiation time-degradation kinetics. The performance of the catalysts was evaluated through a series of degradation experiments. Firstly, the effect of irradiation time was examined. All the composites were put under stirring for 30 minutes with the dye solutions in order for the system to reach equilibrium (shaded area). Then, irradiation under visible light began and measurements every 15 minutes were taken. For VBR, Fig. 5(a), it can be observed that the materials without PyP exhibited a removal of less than 50% within 210 minutes. However, the composites with PyP showed a remarkably increased removal efficiency and rapid kinetics. Especially, CPGNiO(5%)PyP(1%) removed about 80% in the first 60 minutes and reached equilibrium at 180 minutes. The highest degradation ability was exhibited by CPGNiO(5%)PyP(1%) reaching a $R\% = 95\%$, followed by CPGNiO(5%)PyP(0.5%). The Langmuir–Hinshelwood kinetics model following first-order kinetics was applied for the photocatalytic degradation of VBR. All the studied materials showed high correlation coefficient, and their kinetic constants (k_1) were calculated and presented in Table 2. As expected, the highest k_1 was achieved by CPGNiO(5%)PyP(1%) reaching 0.015 min^{-1}, a value triple than CPGNiO(10%)PyP(0.5%) (0.00517 min^{-1}) and almost double than CPGNiO(5%)PyP(0.5%) (0.00861 min^{-1}).

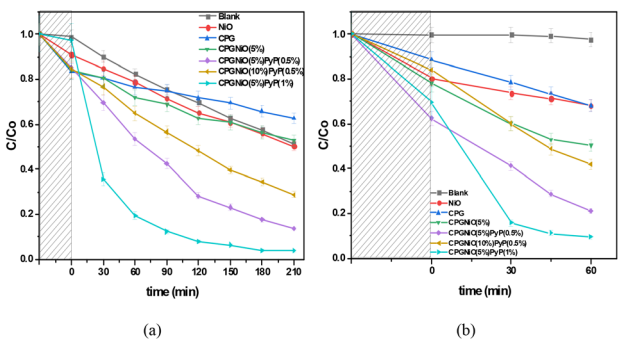

Fig. 5 Degradation kinetics of (a) VBR, (b) RB5 (pH 7, dosage: 0.5 g L^{-1}).

Table 2 Kinetic parameters for the degradation of VBR and RB5

Material	k_1 (min^{-1})	R^2	RRem removal(%)
VBR			
CPG	0.00164	0.9225	37.4
NiO	0.00282	0.9982	49.8
CPGNiO(5%)	0.00248	0.9741	47.2
CPGNiO(5%)PyP(0.5%)	0.00861	0.9929	86.2
CPGNiO(10%)PyP(0.5%)	0.00517	0.9967	72.1
CPGNiO(5%)PyP(1%)	0.01500	0.9585	96.3
RB5			
CPG	0.00419	0.9970	31.9
NiO	0.00407	0.9365	31.9
CPGNiO(5%)	0.00792	0.9897	49.5
CPGNiO(5%)PyP(0.5%)	0.01698	0.9903	78.9
CPGNiO(10%)PyP(0.5%)	0.00996	0.9807	58.0
CPGNiO(5%)PyP(1%)	0.02937	0.9470	90.5

In the case of RB5, a similar trend was observed with CPGNiO(5%)PyP(1%) and CPGNiO(5%)PyP(0.5%) being again the best materials achieving over 80% degradation, Fig. 5(b). This time faster reactions occurred, with the composites reaching equilibrium within 1 h. Again, the Langmuir–Hinshelwood kinetics model was examined and the k_1 were calculated. The values obtained were far greater than those of VBR, with the highest being 0.02937 min^{-1} for CPGNiO(5%)PyP(1%).

The NiO content significantly influenced the photocatalytic degradation efficiency of both VBR and RB5 (Fig. 5). Moderate incorporation of NiO (5 wt%) enhanced photocatalytic activity under visible light irradiation. However, a further increase to 10 wt% NiO led to a noticeable decline in degradation efficiency for both dyes. This reduction in photocatalytic performance at higher NiO content can be attributed to several interrelated factors. Excessive loading of NiO nanoparticles tends to cover the surface of the CPG matrix, including the active porphyrin-based photosensitizing sites. This coverage hinders light absorption at the catalyst interface, thereby impairing the excitation of the photosensitizer. As a result, the generation of reactive oxygen species (ROS) is suppressed, reducing the overall efficiency of the photocatalytic process. In addition, the aggregation of excess NiO particles leads to a decrease in the effective surface area and limits intimate contact between NiO and the underlying matrix, thus inhibiting interfacial charge transfer. Similar effects have been reported in the literature, where agglomerated NiO weakened physical integration with Fe_2O_3, leading to reduced charge separation and photocatalytic performance.[78] Moreover, larger NiO agglomerates tend to act as recombination centers, promoting the rapid recombination of photogenerated electron–hole pairs—another factor that further diminishes photocatalytic activity.[79] These observations collectively explain the activity trend observed with increasing NiO content: while moderate NiO loading promotes charge separation and enhances visible light absorption, excessive amounts adversely affect performance due to aggregation, light shielding, and increased charge recombination.

The π–π interactions between the aromatic rings of the dyes and the graphene oxide moieties, as well as electrostatic

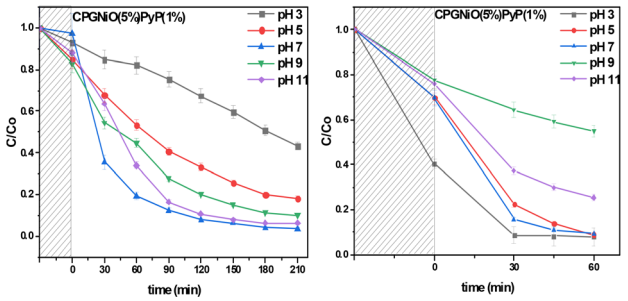

Fig. 6 Effect of pH on degradation of (a) VBR, (b) RB5 (dosage: 0.5 g L^{-1}, shaded area: equilibrium period).

attractions, are key factors in the observed adsorption capacity. For RB5 (an anionic dye), the interaction with the positively charged sites (due to TMPyP and NiO) appears to enhance adsorption, especially in CPGNiO(5%)PyP(1%). Compared the behavior towards VBR and RB5, observing that while VBR removal is predominantly photocatalytic due to its cationic nature and favorable photodegradation pathway, RB5 shows a more significant adsorption component. This difference likely arises from the dye charge, molecular structure, and interaction with the material's functional groups.

3.2.2 Effect of pH. The pH of the solution is a vital parameter in the photocatalysis process, because it can affect the performance of the catalyst by altering its surface charge.[80] In this study, 5 different pH values (3–11) were examined with the same increment step. For the adjustment, 0.1 M HCl and 0.1 M NaOH were used. As it can be seen in Fig. 6(a), the removal of VBR is favoured in neutral to alkaline media. At these levels, the surface of the both dye (pK_a 4.24) and the catalyst are expected to be negatively charged.[81] It can be observed that faster kinetics were achieved at pH 11 in the first 60 minutes, but the removal efficiencies at pH 7 and pH 11 have been almost similar, eliminating >90% of the particular dye. For this reason, pH 7 was selected as the optimal pH value for the rest of the experiments.

For RB5, Fig. 6(b) shows that at pH 3, during the equilibrium period almost 60% of the dye was removed. After irradiation, the process was favoured at acidic to neutral environment, since pH values of 3, 5 and 7 have the same degradation capabilities at 60 minutes, more than 90% degradation of RB5. In contrast, alkaline media reduces significantly the efficiency of the material, especially at pH 9 the removal efficiency is only ~40%. The latter can be attributed to the repulsive forces between the catalyst and dye molecules.[82] Thus, pH 7 was again selected as the optimal value. Table 3 presents the effect of pH on the degradation rate. For VBR pH 7 and 11 exhibited the fastest kinetics, significantly higher than the other conditions, with the lowest k_1 observed at pH 3. In contrast, RB5 showed higher k_1 values at the pH range of 3–7, with only minor differences among these values.

3.2.3 Effect of dosage. Another critical parameter is the dosage of the catalyst. Four different amounts of CPGNiO(5%)PyP(1%) were selected and examined, at the optimal pH values for VBR (Fig. 7(a)) and RB5 (Fig. 7(b)). This is highly significant in photocatalytic research investigations, because it assists to build a cost–effectiveness relationship and avoid decreased removals owing to catalyst aggregation and sedimentation. For both cases, by increasing the concentration of the catalyst the removal % increased, as well as faster kinetics were achieved. A greater catalyst dose increases the surface area accessible for catalyst interactions, as well as the concentration of free radicals in the solution.[83,84] This leads to a higher proportion of dye removal. The best results were obtained from 5 and 10 mg of the material, which presented the same removal efficiency when equilibria were reached. For this reason, the dosage of 5 mg was selected as the optimal for the rest of the experiments. Table 4 presents the effect of catalyst mass on the kinetic constant. For VBR, it was observed that increasing the catalyst dosage led to an increase in the k_1 value which reached a plateau at 5 mg. Upon further increase to 10 mg, a slight decrease in the reaction rate was observed. A similar trend was observed for RB5 removal, with 5 mg again exhibiting the fastest kinetics.

3.2.4 Reusability. Reusability of the catalyst is vital in the practical application of photocatalysts. Previous studies have shown that the efficiency of the photocatalysts gradually fells

Table 3 Effect of pH on the photocatalytic rate constant k_1 of both dyes

pH	k_1 (min^{-1})	R^2	RRem removal (%)
VBR			
3	0.00337	0.9646	56.7
5	0.00752	0.9952	81.7
7	0.01500	0.9584	96.3
9	0.01022	0.9893	89.8
11	0.01341	0.9530	93.6
RB5			
3	0.03074	0.9262	91.9
5	0.02817	0.9694	91.0
7	0.02937	0.9469	90.5
9	0.00663	0.9899	45.1
11	0.01632	0.9758	74.5

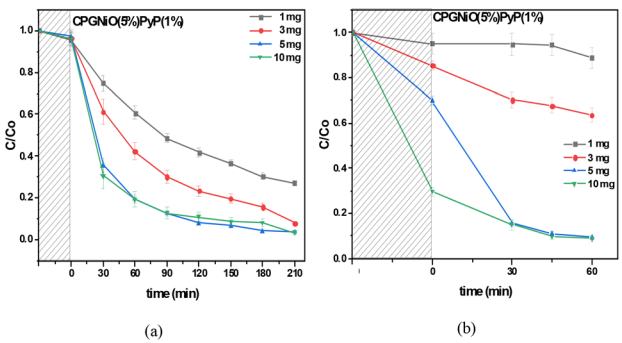

Fig. 7 Effect of catalyst dosage on degradation of (a) VBR, (b) RB5 (pH 7, shaded area: equilibrium period).

Table 4 Effect of dosage on the photocatalytic rate constant k_1 of both dyes

Dosage (mg)	k_1 (min^{-1})	R^2	RRem removal(%)
VBR			
1	0.00581	0.9900	72.9
3	0.01025	0.9774	90.2
5	0.01500	0.9584	96.3
10	0.01342	0.9303	96.7
RB5			
1	0.00105	0.7874	11.3
3	0.00516	0.9884	35.6
5	0.02937	0.9469	90.5
10	0.02729	0.9662	91.2

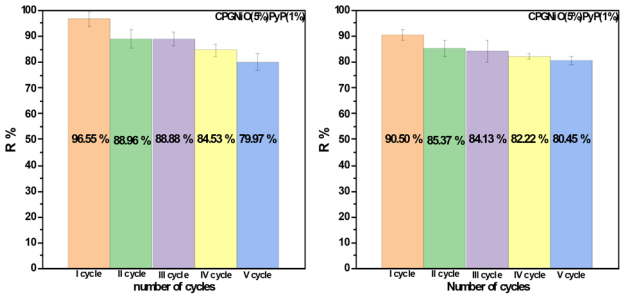

(a) (b)

Fig. 8 Catalyst reusability for (a) VBR, (b) RB5 (pH 7, dosage: 0.5 g L^{-1}).

after each cycle.[85,86] In the case of VBR, Fig. 8(a), CPGNiO(5%) PyP(1%) seemed extremely stable, maintaining its excellent performance for five cycles, losing only 16% of its initial performance. The same trend was followed for the removal of RB5, Fig. 8(b). The catalyst lost 5% of its efficiency in the second cycle and then stabilized at 80–85% *R*% up to the fifth cycle. The reduction in both cases could be explained by the occupied active sites by the adsorption of each dye on the composite's surface.[87,88] Another reason may be the mass loss after each cycle, mainly to the centrifugation process to collect the material. This comes in agreement with the FT-IR studies after photocatalysis, which showed that the composite maintained its structural integrity.

After 4 h of photocatalysis, the FT-IR spectra of CPGNiO(5%) PyP(1%) show that the functional groups still exist, with lower intensity (Fig. S2). The lower intensity may be due to the reduction in the number of functional groups of the material.[89] However, it does not dramatically affect the photocatalysis process, since it can be reused up to 5 times with a degradation efficiency of up to 80%, according to the photocatalytic cycles of Fig. 7.

3.2.5 Mixtures study. The effectiveness of CPGNiO(5%) PyP(1%) towards binary dye mixtures was also examined, with various VBR/RB5 ratios and the results are presented in Fig. 9(a–c). In all studied cases, the catalyst kept its high performance, eliminating more than 76% of both dyes. By increasing the RB5 quantity in the solution, the removal efficiency decreased. At pH

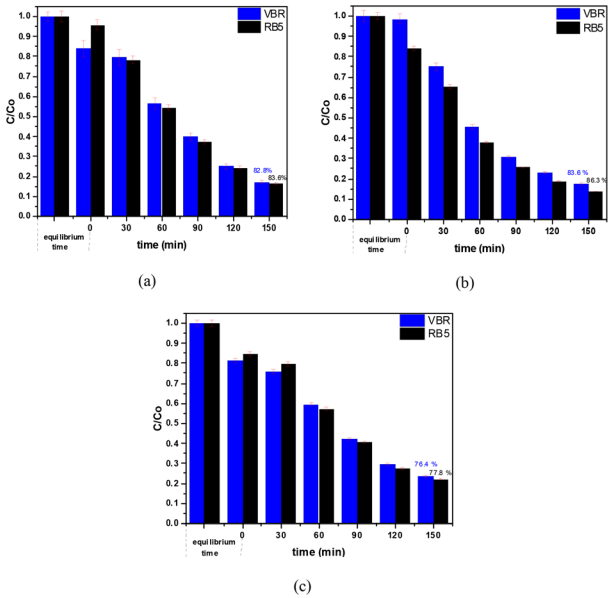

(a) (b) (c)

Fig. 9 Double dye degradation efficiency for VBR : RB5 ratios (a) 1 : 1, (b) 2 : 1, (c) 1 : 2.

7, VBR is negatively charged (pK_a 4.24), as well as RB5 is slightly negatively charged (pK_a 3.8 and 6.9). Thus, these interactions between two dyes could possibly hinder the degradation efficiency. Similar behaviour was observed in other studies.[90–92]

3.2.6. Mechanism of photocatalytic degradation of dyes. Experiments with various radical scavengers were performed to examine the role of active species in degradation of VBR and RB5. The trapping agents used were ethylenediamine tetraacetic acid (EDTA) as a hole (h^+) scavenger, isopropanol (IPA) as a hydroxyl radical ($^{\bullet}OH$) scavenger, acrylamide (AC) as superoxide radical ($^{\bullet}O_2^-$) scavenger and silver nitrate ($AgNO_3$) as electron (e^-) scavenger. The effects of these scavengers on the photodegradation of VBR and RB5 are presented in Fig. 10a and b, respectively. The addition of EDTA significantly suppressed the degradation of VBR confirming that photogenerated holes (h^+) play a dominant role in its oxidative degradation. In contrast, for RB5, the presence of EDTA was unexpectedly enhanced the dye degradation. This suggests that EDTA does

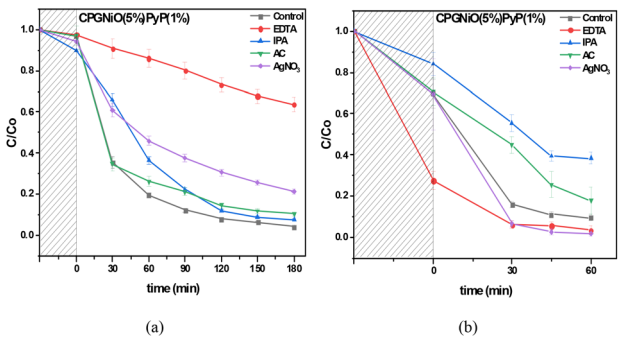

(a) (b)

Fig. 10 Scavenger effect on photodegradation of (a) VBR, (b) RB5 (shaded area: equilibrium period).

not act primarily as a hole scavenger. Instead, it may enhance degradation by preventing electron–hole recombination through hole capture, thus prolonging the lifetime of electrons. These electrons can subsequently reduce O_2 to superoxide radicals ($^{\bullet}O_2^-$), which contribute indirectly to dye oxidation.[93] The use of IPA and AC had negligible effects on the degradation of VBR, whereas for RB5, both caused moderate inhibition, implying the partial involvement of $^{\bullet}OH$ and $^{\bullet}O_2^-$ radicals in its degradation pathway. Electron scavenging using $AgNO_3$ resulted in modest suppression of VBR degradation, suggesting that although electrons are not the primary reactive species, they do contribute to the generation of secondary oxidants such as $^{\bullet}O_2^-$ and $^{\bullet}OH$. These findings point toward a multi-pathway photocatalytic mechanism for both dyes.

In the case of VBR, hole-mediated oxidation appears to be the dominant pathway, supported by electron–driven processes. For RB5, the mechanism is primarily driven by $^{\bullet}OH$ radicals, with additional contribution from superoxide species. These mechanistic insights highlight the well-optimized and synergistic architecture of the CPGNiO(5%)PyP(1%) composite. The intimate interaction between nickel oxide, the porphyrin photosensitizer, GO and CS-PVA polymer matrix promotes efficient charge separation, effectively minimizing electron–hole recombination. The composite's structural configuration ensures the availability of photogenerated holes at the surface for direct pollutant oxidation, while also facilitating the generation of reactive oxygen species such as $^{\bullet}OH$ and $^{\bullet}O_2^-$ through enhanced electron transfer effects amplified by the conductive and catalytic properties of GO and NiO. This integrated, multi-pathway mechanism underlies the robust and sustained photocatalytic activity observed for both dye systems.

The photocatalytic performance of CPGNiO(5%)PyP(1%) was systematically evaluated using VBR and RB5 dyes under different degradation mechanisms: adsorption, photolysis, and photocatalysis (Fig. 11). In the case of VBR, the adsorption process resulted in only a slight decrease in dye concentration over 210 minutes, suggesting minimal dye removal through surface interactions alone. Photolysis caused a gradual reduction in dye concentration, indicating moderate degradation due to light-induced processes in the absence of a catalyst. In contrast, the photocatalytic process exhibited rapid dye degradation, achieving nearly complete removal within 150 minutes, thereby highlighting the superior efficiency of the photocatalyst in generating reactive species under light irradiation.

For RB5, photolysis had a negligible effect, with dye degradation remaining nearly unchanged, whereas adsorption resulted in a 44% removal of the dye. The photocatalysis pathway, however, achieved rapid and near-complete degradation of RB5 within 60 minutes. These results underscore the crucial role of CPGNiO(5%)PyP(1%) as an effective visible-light-responsive photocatalyst, with both high electron–hole separation efficiency and optimal dye–surface interaction facilitating significant pollutant breakdown across varied dye structures.

To conclude, the combined mechanistic and performance insights clearly highlight the synergistic efficacy of the CPGNiO(5%)PyP(1%) composite. While adsorption and photolysis separately proved only modestly effective, the photocatalytic process, powered by efficient electron–hole separation and robust visible-light absorption, drove a rapid and near-complete degradation of both VBR and RB5. Mechanistic studies confirm that both dyes are primarily oxidized by photogenerated holes. Additionally, the cationic dye VBR undergoes degradation through electron-mediated processes, while the anionic dye RB5 is mainly decomposed *via* superoxide radicals.[94,95] In the case of RB5, adsorption onto the composite played a significant role in dye removal, which was subsequently enhanced by photocatalysis. This behaviour is attributed to favourable electrostatic interactions between the anionic dye and the surface of the material. Altogether, these findings confirm that the tailored architecture of NiO, porphyrin, GO, and chitosan-graphene oxide in CPGNiO(5%)PyP(1%) enables a potent, multi-pathway photocatalytic mechanism that is highly effective across diverse dye types under visible light irradiation. The mechanism of charge transfer within the material upon excitation, as well as the associated photocatalytic process, is depicted in Fig. 12.

The photocatalytic activity of the CPGNiO(5%)PyP(1%) composite was initiated upon exposure to visible light, which

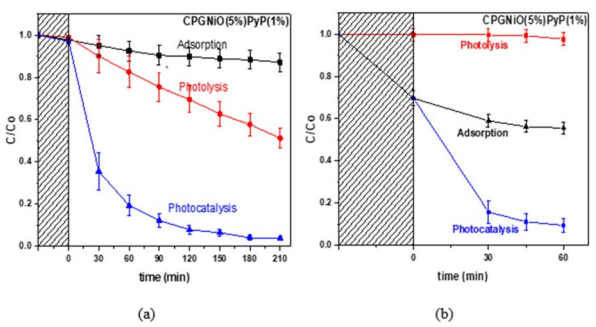

Fig. 11 Comparison of degradation mechanisms (adsorption, photolysis, photocatalysis) for (a) VBR, (b) RB5 (shaded area: equilibrium period).

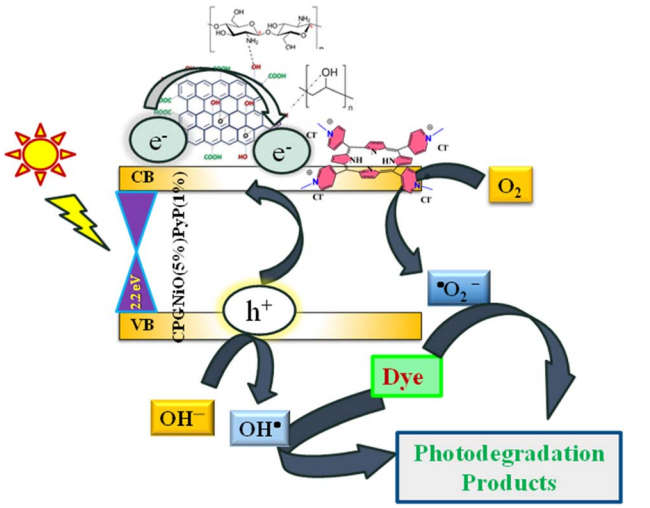

Fig. 12 Proposed photocatalytic degradation mechanism of CPGNiO(5%)PyP(1%) under visible light.

Table 5 Comparison of recent visible-light-responsive photocatalysts for dye degradation

Material	Target dye (s)	Visible-light efficiency	Reusability	Key mechanism	Ref
CPGNiO(5%)PyP(1%), (This work)	Victoria blue R (96.3%), reactive black 5 (90.5%)	Excellent (≥90%) under visible light	>80% activity retained after 5 cycles; effective in dye mixtures	Porphyrin photosensitization, NiO-driven ROS generation ($^{\bullet}OH$, $^{\bullet}O_2^-$, h^+)	This study
rGO/Ni-BDP	Methyl orange	86.2% (pH 3, visible light)	Moderate loss over 5 cycles	π–π interaction, porphyrin sensitization, rGO conductivity	96
MRGO 20 (rGO/$Zn_{0.5}Cu_{0.5}Fe_2O_4$)	Methyl orange	96% in 40 min (pH 5)	High retention after 5 cycles	Charge transfer *via* rGO, enhanced radical formation by ferrite	97
rGO/NiO/Ag	Methylene blue	High under solar simulator	Maintains activity across cycles	Ag plasmonic effect + NiO light absorption + e^-/h^+ separation	98
GO/NiO nanocomposite	Methylene blue and methyl orange	~100% degradation (high efficiency claim)	Not clearly specified	GO enhances dispersion; NiO absorbs visible light	44
g-C_3N_4@V_2C MXene	Methyl orange	94.5% (≈ 1.56× g-C_3N_4)	>85% after 3 cycles	MXene improves charge transfer, suppresses recombination	99

induced the generation of electron–hole pairs. Photoexcited electrons migrated to the conduction band (CB), while the corresponding holes remained in the valence band (VB), as illustrated in eqn (3). These conduction band electrons subsequently reacted with molecular oxygen to form superoxide radicals ($^{\bullet}O_2^-$), whereas the valence band holes oxidized surface hydroxyl groups or water molecules to produce hydroxyl radicals ($^{\bullet}OH$), as described in eqn (4)–(6). These reactive oxygen species (ROS), including $^{\bullet}O_2^-$ and $^{\bullet}OH$, are primarily responsible for the degradation of dye molecules, as represented by eqn (7) and (8).

$$\text{CPGNiO(5\%)PPyP(1\%)} + h\nu \rightarrow e^-_{(CB)} + h^+_{(VB)} \quad (3)$$

$$e^- + O_2 \rightarrow {}^{\bullet}O_2^- \quad (4)$$

$$h^+ + OH^- \rightarrow {}^{\bullet}OH \quad (5)$$

$$h^+ + H_2O \rightarrow {}^{\bullet}OH + H^+ \quad (6)$$

$$^{\bullet}OH + \text{dye} \rightarrow CO_2 + H_2O + \text{photodegradation products} \quad (7)$$

$$^{\bullet}O_2^- + \text{dye} \rightarrow CO_2 + H_2O + \text{photodegradation products} \quad (8)$$

The band gap of the composite was determined to be approximately 2.2 eV, confirming its ability to harness light from the visible region of the electromagnetic spectrum. This visible-light-responsive behavior, combined with the composite's photostability under experimental conditions, enabled efficient photocatalytic performance. Moreover, the catalyst demonstrated excellent reusability over multiple photocatalytic cycles without significant loss in activity, highlighting its potential for sustainable applications in pollutant degradation.

To better situate our work within the current research landscape, we compared the performance of the CPGNiO(5%)PyP(1%) composite with several recent visible-light-responsive photocatalysts (Table 5). Notably, our system achieved high degradation efficiencies for both cationic (Victoria Blue R, 96.3%) and anionic (Reactive Black 5, 90.5%) dyes, which is comparable or superior to many state-of-the-art materials such as rGO/Ni-BDP (86.2% for Methyl Orange) and MRGO/$Zn_{0.5}Cu_{0.5}Fe_2O_4$ (96% for Methyl Orange). While other systems often focus on single dye types or require acidic conditions, our composite demonstrates broad-spectrum activity, strong reusability (retaining >80% activity after five cycles), and effectiveness in multi-dye environments under visible light. These advantages are attributed to the synergistic integration of NiO nanoparticles and a porphyrin-based photosensitizer within a graphene oxide–chitosan aerogel matrix, which promotes efficient charge separation and reactive oxygen species (ROS) generation. This comparison highlights the promising potential of our CPGNiO(5%)PyP(1%) composite as a scalable, sustainable solution for wastewater treatment.

4. Conclusions

In this study, a novel, visible-light-responsive photocatalyst was successfully developed by integrating nickel oxide nanoparticles

and a porphyrin photosensitizer into a chitosan–graphene oxide aerogel matrix. Among the synthesized materials, the CPGNiO(5%)PyP(1%) composite exhibited outstanding photocatalytic activity, achieving high degradation efficiencies for both cationic (Victoria Blue R) and anionic (Reactive Black 5) dyes. This enhanced performance is attributed to the synergistic interaction between the components, which promotes effective charge separation and facilitates the generation of reactive oxygen species under visible-light irradiation. Mechanistic investigations revealed distinct degradation pathways for each dye, highlighting the role of photogenerated holes, hydroxyl, and superoxide radicals. The composite also demonstrated excellent stability and reusability, maintaining over 80% of its activity after five cycles, and performed effectively in a double dye system, underscoring its practical applicability. Overall, the tailored multi-component architecture of CPGNiO(5%)PyP(1%) offers a promising platform for solar-driven wastewater treatment. Its ease of fabrication, strong visible-light activity, and broad-spectrum dye degradation capabilities position it as a scalable and sustainable solution for addressing dye pollution.

Author contributions

A. Faraos, conceptualization, investigation, formal analysis; K. N. Maroulas, conceptualization, investigation, methodology, formal analysis, writing – original draft; E. Nikoloudakis, formal analysis, investigation; C. Drivas, formal analysis, investigation; writing – original draft; M. A. Isaacs, formal analysis, investigation; writing – original draft; G. Z. Kyzas, data curation, methodology, writing – original draft, writing – review & editing; K. Ladomenou, conceptualization curation, methodology, writing – original draft, writing – review & editing.

Conflicts of interest

There are no conflicts to declare.

Data availability

All data generated or analysed in this study are included in this article and at the SI. Any additional data related to this paper may be requested from the corresponding author: kladomenou@chem.duth.gr.

Supplementary information is available. See DOI: **https://doi.org/10.1039/d5ra04647e**.

Acknowledgements

Funding: "Advanced Nanostructured Materials for Sustainable Growth: Green Energy Production/Storage, Energy Saving and Environmental Remediation" (TAEDR-0535821) which is implemented under the action "Flagship actions in interdisciplinary scientific fields with a special focus on the productive fabric" (ID 16618), Greece 2.0 – National Recovery and Resilience Fund and funded by European Union NextGenerationEU. X-ray photoelectron (XPS) data were acquired at the UK EPSRC National Facility for XPS ("HarwellXPS", EP/Y023587/1, EP/Y023609/1, EP/Y023536/1, EP/Y023552/1 and EP/Y023544/1); E. Nikoloudakis gratefully acknowledges the Bodossaki Foundation for financial support.

References

1 A. Bafana, S. S. Devi and T. Chakrabarti, Azo dyes: past, present and the future, *Environ. Rev.*, 2011, **19**, 350–371.
2 S. Sudarshan, S. Harikrishnan, G. RathiBhuvaneswari, V. Alamelu, S. Aanand, A. Rajasekar and M. Govarthanan, Impact of textile dyes on human health and bioremediation of textile industry effluent using microorganisms: current status and future prospects, *J. Appl. Microbiol.*, 2023, **134**, lxac064.
3 T. Islam, Md. R. Repon, T. Islam, Z. Sarwar and M. M. Rahman, Impact of textile dyes on health and ecosystem: a review of structure, causes, and potential solutions, *Environ. Sci. Pollut. Res.*, 2023, **30**, 9207–9242.
4 D. Goswami, J. Mukherjee, C. Mondal and B. Bhunia, Bioremediation of azo dye: A review on strategies, toxicity assessment, mechanisms, bottlenecks and prospects, *Sci. Total Environ.*, 2024, **954**, 176426.
5 A. I. Khedr and M. H. H. Ali, Eco-friendly fabrication of copper oxide nanoparticles using peel extract of Citrus aurantium for the efficient degradation of methylene blue dye, *Sci. Rep.*, 2024, **14**, 29156.
6 A. Singh, D. B. Pal, A. Mohammad, A. Alhazmi, S. Haque, T. Yoon, N. Srivastava and V. K. Gupta, Biological remediation technologies for dyes and heavy metals in wastewater treatment: New insight, *Bioresour. Technol.*, 2022, **343**, 126154.
7 A. K. Sahoo, A. Dahiya and B. K. Patel, in *Development in Wastewater Treatment Research and Processes*, ed. M. P. Shah, S. Rodriguez-Couto and R. T. Kapoor, Elsevier, 2022, pp. 127–151.
8 Y. Shi, Q. Chang, T. Zhang, G. Song, Y. Sun and G. Ding, A review on selective dye adsorption by different mechanisms, *J. Environ. Chem. Eng.*, 2022, **10**, 108639.
9 S. Singh, V. C. Srivastava and I. D. Mall, Mechanism of Dye Degradation during Electrochemical Treatment, *J. Phys. Chem. C*, 2013, **117**, 15229–15240.
10 S. Khan, T. Noor, N. Iqbal and L. Yaqoob, Photocatalytic Dye Degradation from Textile Wastewater: A Review, *ACS Omega*, 2024, **9**, 21751–21767.
11 S. Taghavi Fardood, S. Ganjkhanlu, F. Moradnia and A. Ramazani, Green synthesis, characterization, and photocatalytic activity of superparamagnetic MgFe2O4@ZnAl2O4 nanocomposites, *Sci. Rep.*, 2024, **14**, 16670.
12 S. S. Wagh, A. S. Chougale, A. A. Survase, R. S. Patil, N. Naik, M. Naushad and H. M. Pathan, Rapid photocatalytic dye degradation, enhanced antibacterial and antifungal activities of silver stacked zinc oxide garnished on carbon nanotubes, *Sci. Rep.*, 2024, **14**, 14045.
13 V. Hasija, P. Raizada, A. Sudhaik, K. Sharma, A. Kumar, P. Singh, S. B. Jonnalagadda and V. K. Thakur, Recent

advances in noble metal free doped graphitic carbon nitride based nanohybrids for photocatalysis of organic contaminants in water: A review, *Appl. Mater. Today*, 2019, **15**, 494–524.

14 N. Miranda-García, S. Suárez, M. I. Maldonado, S. Malato and B. Sánchez, Regeneration approaches for TiO2 immobilized photocatalyst used in the elimination of emerging contaminants in water, *Catal. Today*, 2014, **230**, 27–34.

15 Z. Long, Q. Li, T. Wei, G. Zhang and Z. Ren, Historical development and prospects of photocatalysts for pollutant removal in water, *J. Hazard. Mater.*, 2020, **395**, 122599.

16 G. Salehi, M. Bagherzadeh, R. Abazari, M. Hajilo and D. Taherinia, Visible Light-Driven Photocatalytic Degradation of Methylene Blue Dye Using a Highly Efficient Mg–Al LDH@g-C_3N_4@Ag_3PO_4 Nanocomposite, *ACS Omega*, 2024, **9**, 4581–4593.

17 X. Zhou, T. Wang, D. He, P. Chen, H. Liu, H. Lv, H. Wu, D. Su, H. Pang and C. Wang, Efficient Photocatalytic Desulfurization in Air through Improved Photogenerated Carriers Separation in MOF MIL101/Carbon Dots-g-C_3N_4 Nanocomposites, *Angew. Chem., Int. Ed.*, 2024, **63**, e202408989.

18 X. Yang, J. Peng, L. Zhao, H. Zhang, J. Li, P. Yu, Y. Fan, J. Wang, H. Liu and S. Dou, Insights on advanced g-C_3N_4 in energy storage: Applications, challenges, and future, *Carbon Energy*, 2024, **6**, e490.

19 J. Wang and S. Wang, A critical review on graphitic carbon nitride (g-C_3N_4)-based materials: Preparation, modification and environmental application, *Coord. Chem. Rev.*, 2022, **453**, 214338.

20 R. Tao, S. Yang, C. Shao, X. Li, X. Li, S. Liu, J. Zhang and Y. Liu, Reusable and Flexible g-C_3N_4/Ag_3PO_4/Polyacrylonitrile Heterojunction Nanofibers for Photocatalytic Dye Degradation and Oxygen Evolution, *ACS Appl. Nano Mater.*, 2019, **2**, 3081–3090.

21 T. Garg, Nitansh, A. Goyal, A. Kaushik and S. Singhal, State-of-the-art evolution of g-C_3N_4 based Z-scheme heterostructures towards energy and environmental applications: A review, *Mater. Res. Bull.*, 2023, **168**, 112448.

22 Y. Gong, J. Wang, Z. Wei, P. Zhang, H. Li and Y. Wang, Combination of Carbon Nitride and Carbon Nanotubes: Synergistic Catalysts for Energy Conversion, *ChemSusChem*, 2014, **7**, 2303–2309.

23 D.-E. Lee, M.-K. Kim, M. Danish and W.-K. Jo, State-of-the-art review on photocatalysis for efficient wastewater treatment: Attractive approach in photocatalyst design and parameters affecting the photocatalytic degradation, *Catal. Commun.*, 2023, **183**, 106764.

24 K. P. Makhado, M. M. Mphahlele-Makgwane, N. Kumar, P. G. L. Baker and P. R. Makgwane, Current updates on p-type nickel oxide (NiO) based photocatalysts towards decontamination of organic pollutants from wastewater, *Mater. Today Sustain.*, 2024, **25**, 100664.

25 N. Singh, S. Riyajuddin, K. Ghosh, S. K. Mehta and A. Dan, Chitosan-Graphene Oxide Hydrogels with Embedded Magnetic Iron Oxide Nanoparticles for Dye Removal, *ACS Appl. Nano Mater.*, 2019, **2**, 7379–7392.

26 S. R. D. Gamelas, J. P. C. Tomé, A. C. Tomé and L. M. O. Lourenço, Porphyrin-containing materials for photodegradation of organic pollutants in wastewaters: a review, *Catal. Sci. Technol.*, 2024, **14**, 2352–2389.

27 D. A. Gkika, K. Ladomenou, M. Bououdina, A. C. Mitropoulos and G. Z. Kyzas, Adsorption and photocatalytic applications of porphyrin-based materials for environmental separation processes: A review, *Sci. Total Environ.*, 2024, **908**, 168293.

28 N. El-Shafai, M. E. El-Khouly, M. El-Kemary, M. S. Ramadan and M. S. Masoud, Self-assembly of porphyrin on graphene oxide in aqueous medium: fabrication, characterization, and photocatalytic studies, *Photochem. Photobiol. Sci.*, 2019, **18**, 2071–2079.

29 A. M. Kobaisy, M. F. Elkady, A. A. Abdel-Moneim and M. E. El-Khouly, Surface-decorated porphyrinic zirconium-based metal–organic frameworks (MOFs) using post-synthetic self-assembly for photodegradation of methyl orange dye, *RSC Adv.*, 2023, **13**, 23050–23060.

30 S. (Gabriel) Kou, L. M. Peters and M. R. Mucalo, Chitosan: A review of sources and preparation methods, *Int. J. Biol. Macromol.*, 2021, **169**, 85–94.

31 K. S. Venkataprasanna, J. Prakash, S. Vignesh, G. Bharath, M. Venkatesan, F. Banat, S. Sahabudeen, S. Ramachandran and G. Devanand Venkatasubbu, Fabrication of Chitosan/PVA/GO/CuO patch for potential wound healing application, *Int. J. Biol. Macromol.*, 2020, **143**, 744–762.

32 A. M. Ali, S. M. Elshabrawy and E. A. Kamoun, Evaluation of the mechanical properties and degradation behavior of chitosan-PVA-graphene oxide nanocomposite scaffolds in vitro, *J. Taibah Univ. Med. Sci.*, 2024, **19**, 585–597.

33 L. Das, P. Das, A. Bhowal and C. Bhattachariee, Synthesis of hybrid hydrogel nano-polymer composite using Graphene oxide, Chitosan and PVA and its application in waste water treatment, *Environ. Technol. Innovat.*, 2020, **18**, 100664.

34 V. Nikolaou, E. Nikoloudakis, K. Ladomenou, G. Charalambidis and A. G. Coutsolelos, Porphyrins—valuable pigments of life, *Front. Chem. Biol*, 2024, **2**, 1346465.

35 A. Tsoupras, S. Pafli, C. Stylianoudakis, K. Ladomenou, C. A. Demopoulos and A. Philippopoulos, Anti-Inflammatory and Antithrombotic Potential of Metal-Based Complexes and Porphyrins, *Compounds*, 2024, **4**, 376–400.

36 A. Charisiadis, V. Nikolaou, E. Nikoloudakis, K. Ladomenou, G. Charalambidis and A. G. Coutsolelos, Metalloporphyrins in bio-inspired photocatalytic conversions, *Chem. Commun.*, 2025, **61**, 4630–4646.

37 E. Nikoloudakis, I. López-Duarte, G. Charalambidis, K. Ladomenou, M. Ince and A. G. Coutsolelos, Porphyrins and phthalocyanines as biomimetic tools for photocatalytic H_2 production and CO_2 reduction, *Chem. Soc. Rev.*, 2022, **51**, 6965–7045.

38 S. Ardebilchi Marand, H. Almasi and N. Ardebilchi Marand, Chitosan-based nanocomposite films incorporated with NiO nanoparticles: Physicochemical, photocatalytic and

antimicrobial properties, *Int. J. Biol. Macromol.*, 2021, **190**, 667–678.

39 S. H. El-Khalafy, M. T. Hassanein, M. M. Alaskary and N. A. Salahuddin, Synthesis and characterization of Co(II) porphyrin complex supported on chitosan/graphene oxide nanocomposite for efficient green oxidation and removal of Acid Orange 7 dye, *Sci. Rep.*, 2024, **14**, 17073.

40 Y. Cheng, B. Liang, J. Chao, X. Wei, S.-D. Li, P. Wang and D. Xia, A Supramolecular Polymer Network Based on Chitosan and Porphyrin and Its Application as an Adsorbent for Selective Removal of Dyes from Water, *Adv. Sustainable Syst.*, 2024, **8**, 2400291.

41 M. L. Tran, T. T. V. Tran, R.-S. Juang and C. H. Nguyen, Graphene oxide crosslinked chitosan composites for enhanced adsorption of cationic dye from aqueous solutions, *J. Taiwan Inst. Chem. Eng.*, 2023, **142**, 104678.

42 M. Sabzevari, D. E. Cree and L. D. Wilson, Graphene Oxide–Chitosan Composite Material for Treatment of a Model Dye Effluent, *ACS Omega*, 2018, **3**, 13045–13054.

43 M. H. El-Newehy, A. Aldalbahi, B. M. Thamer and M. M. Abdulhameed, Photocatalytic degradation of methylene blue using chitosan/NiO nanocomposite: A comprehensive exploration, *Opt. Mater.*, 2024, **152**, 115531.

44 M. Maruthupandy, T. Muneeswaran, T. Vennila, C. V. Vaishali, M. Anand, W.-S. Cho and F. Quero, Photocatalytic efficiency of graphene/nickel oxide nanocomposites towards the degradation of anionic and cationic dye molecules under visible light, *J. Photochem. Photobiol., A*, 2022, **427**, 113819.

45 Raveena, M. P. Singh, M. Sengar and P. Kumari, Synthesis of Graphene oxide/Porphyrin Nanocomposite for Photocatalytic Degradation of Crystal Violet Dye, *ChemistrySelect*, 2023, **8**, e202203272.

46 A. Panagiotopoulos, K. Ladomenou, D. Sun, V. Artero and A. G. Coutsolelos, Photochemical hydrogen production and cobaloximes: the influence of the cobalt axial N-ligand on the system stability, *Dalton Trans.*, 2016, **45**, 6732–6738.

47 K. N. Maroulas, N. Vordos, A. C. Mitropoulos and G. Z. Kyzas, Nanobubbles in graphene oxide synthesis: investigation of structure and physicochemical properties with boosting of oxygen content and microporous surface area, *RSC Adv.*, 2025, **15**, 16525–16531.

48 H. R. Rajabi, H. Arjmand, H. Kazemdehdashti and M. Farsi, A comparison investigation on photocatalytic activity performance and adsorption efficiency for the removal of cationic dye: Quantum dots *vs.* magnetic nanoparticles, *J. Environ. Chem. Eng.*, 2016, **4**, 2830–2840.

49 I. Shaheen, S. Ata, H. Aslam, H. Farooq, A. Ali, Z. M. Elqahtani, N. Alwadai, M. Iqbal, H. Arif and A. Nazir, Photocatalytic removal of methylene blue and Victoria blue R dyes using Tb and La-doped $BaZnO_2$, *Desalination Water Treat.*, 2024, **318**, 100389.

50 S. Song, L. Xu, Z. He, J. Chen, X. Xiao and B. Yan, Mechanism of the Photocatalytic Degradation of C.I. Reactive Black 5 at pH 12.0 Using SrTiO3/CeO2 as the Catalyst, *Environ. Sci. Technol.*, 2007, **41**, 5846–5853.

51 T. Soltani and M. H. Entezari, Solar photocatalytic degradation of RB5 by ferrite bismuth nanoparticles synthesized *via* ultrasound, *Ultrason. Sonochem.*, 2013, **20**, 1245–1253.

52 F. Puga, J. A. Navío and M. C. Hidalgo, A critical view about use of scavengers for reactive species in heterogeneous photocatalysis, *Appl. Catal., A*, 2024, **685**, 119879.

53 I. Langmuir, The adsorption of gases on plane surfaces of glass, mica and platinum, *J. Am. Chem. Soc.*, 1918, **40**, 1361–1403.

54 N. Syngelaki, S. L. Kouvalakidou, K. N. Maroulas, A. D. Meretoudi, D. G. Trikkaliotis, C. Emmanouil, M. Kostoglou, I. Koumentakou and G. Z. Kyzas, Hybrid composite beads of chitosan/graphene oxide for dye adsorption: characterizations, kinetic modeling and toxicity study, *J. Dispersion Sci. Technol.*, 1–15.

55 K. N. Maroulas, D. G. Trikkaliotis, Z. S. Metaxa, N. AbdelAll, A. Alodhayb, G. A. Khouqeer and G. Z. Kyzas, Super-hydrophobic chitosan/graphene-based aerogels for oil absorption, *J. Mol. Liq.*, 2023, **390**, 123071.

56 M. U. A. Khan, Z. Yaqoob, M. N. M. Ansari, S. I. A. Razak, M. A. Raza, A. Sajjad, S. Haider and F. M. Busra, Chitosan/Poly Vinyl Alcohol/Graphene Oxide Based pH-Responsive Composite Hydrogel Films: Drug Release, Anti-Microbial and Cell Viability Studies, *Polymers*, 2021, **13**, 3124.

57 D. D. Borhade, S. N. Nangare, D. A. Patil, P. O. Patil, G. S. Patil and G. B. Patil, Preparation of pirfenidone loaded chitosan-polyvinyl alcohol-graphene oxide-based scaffold: Spectroscopical characterizations and antibacterial activity, *J. Drug Delivery Sci. Technol.*, 2023, **82**, 104325.

58 R. Gobi and R. S. Babu, *In vitro* study on chitosan/PVA incorporated with nickel oxide nanoparticles for wound healing application, *Mater. Today Commun.*, 2023, **34**, 105154.

59 F. Momtaz, E. Momtaz, M. A. Mehrgardi, M. Momtaz, T. Narimani and F. Poursina, Enhanced antibacterial properties of polyvinyl alcohol/starch/chitosan films with NiO–CuO nanoparticles for food packaging, *Sci. Rep.*, 2024, **14**, 7356.

60 Y. Zheng, H. Ma, J. Wang and C. Fan, Preparation of graphene oxide/carboxymethyl chitosan/polyvinyl alcohol composite nanofiber membranes by electrospinning for heavy metal adsorption, *J. Appl. Polym. Sci.*, 2024, **141**, e54840.

61 T. B. Atisme, C.-Y. Yu, E. N. Tseng, Y.-C. Chen, P.-K. Shu and S.-Y. Chen, Interface Interactions in Conjugated Polymer Composite with Metal Oxide Nanoparticles, *Nanomaterials*, 2019, **9**, 1534.

62 K. A. D. F. Castro, N. M. M. Moura, F. Figueira, R. I. Ferreira, M. M. Q. Simões, J. A. S. Cavaleiro, M. A. F. Faustino, A. J. D. Silvestre, C. S. R. Freire, J. P. C. Tomé, S. Nakagaki, A. Almeida and M. G. P. M. S. Neves, New Materials Based on Cationic Porphyrins Conjugated to Chitosan or Titanium Dioxide: Synthesis, Characterization and Antimicrobial Efficacy, *Int. J. Mol. Sci.*, 2019, **20**, 2522.

63 Y.-B. Tian, N. Vankova, P. Weidler, A. Kuc, T. Heine, C. Wöll, Z.-G. Gu and J. Zhang, Oriented Growth of In-Oxo Chain Based Metal-Porphyrin Framework Thin Film for High-Sensitive Photodetector, *Advanced Science*, 2021, **8**, 2100548.
64 A. Lim Teik Zheng, T. Phromsatit, S. Boonyuen and Y. Andou, Synthesis of silver nanoparticles/porphyrin/reduced graphene oxide hydrogel as dye adsorbent for wastewater treatment, *FlatChem*, 2020, **23**, 100174.
65 M. A. Shamekhi, H. Mirzadeh, H. Mahdavi, A. Rabiee, D. Mohebbi-Kalhori and M. Baghaban Eslaminejad, Graphene oxide containing chitosan scaffolds for cartilage tissue engineering, *Int. J. Biol. Macromol.*, 2019, **127**, 396–405.
66 P.-P. Zuo, H.-F. Feng, Z.-Z. Xu, L.-F. Zhang, Y.-L. Zhang, W. Xia and W.-Q. Zhang, Fabrication of biocompatible and mechanically reinforced graphene oxide-chitosan nanocomposite films, *Chem. Cent. J.*, 2013, **7**, 39.
67 X. Zeng, B. Zhu, W. Qiu, W. Li, X. Zheng and B. Xu, A review of the preparation and applications of wrinkled graphene oxide, *N. Carbon Mater.*, 2022, **37**, 290–302.
68 H. Ali, T. M. Tiama and A. M. Ismail, New and efficient NiO/chitosan/polyvinyl alcohol nanocomposites as antibacterial and dye adsorptive films, *Int. J. Biol. Macromol.*, 2021, **186**, 278–288.
69 E. Salim, A. Magdy, A. H. EL-Farrash and A. El-Shaer, Optimizing optical, dielectric, and electrical properties of polyvinyl alcohol/polyvinyl pyrrolidone/poly(3,4-ethylene dioxythiophene) polystyrene sulfonate/NiO-based polymeric nanocomposites for optoelectronic applications, *Sci. Rep.*, 2025, **15**, 821.
70 A. R. Monteiro, M. G. P. M. S. Neves and T. Trindade, Functionalization of Graphene Oxide with Porphyrins: Synthetic Routes and Biological Applications, *ChemPlusChem*, 2020, **85**, 1857–1880.
71 A. R. Monteiro, C. I. V. Ramos, S. Fateixa, N. M. M. Moura, M. G. P. M. S. Neves and T. Trindade, Hybrids Based on Graphene Oxide and Porphyrin as Tools for Detection and Stabilization of DNA G-Quadruplexes, *ACS Omega*, 2018, **3**, 11184–11191.
72 N. Karousis, A. S. D. Sandanayaka, T. Hasobe, S. P. Economopoulos, E. Sarantopoulou and N. Tagmatarchis, Graphene oxide with covalently linked porphyrin antennae: Synthesis, characterization and photophysical properties, *J. Mater. Chem.*, 2010, **21**, 109–117.
73 D. J. Morgan, Comments on the XPS Analysis of Carbon Materials, *C*, 2021, **7**, 51.
74 J. D. Henderson, B. P. Payne, N. S. McIntyre and M. C. Biesinger, Enhancing Oxygen Spectra Interpretation by Calculating Oxygen Linked to Adventitious Carbon, *Surf. Interface Anal.*, 2025, **57**, 214–220.
75 Q. Dai, J. Zhang and M. Ma, The formation of composites from imidazolate polymer with epoxy resins, *Appl. Surf. Sci.*, 1993, **72**, 67–72.
76 M. C. Biesinger, B. P. Payne, A. P. Grosvenor, L. W. M. Lau, A. R. Gerson and R. St. C. Smart, Resolving surface chemical states in XPS analysis of first row transition metals, oxides and hydroxides: Cr, Mn, Fe, Co and Ni, *Appl. Surf. Sci.*, 2011, **257**, 2717–2730.
77 R. Franke, Th. Chassé, P. Streubel and A. Meisel, Auger parameters and relaxation energies of phosphorus in solid compounds, *J. Electron Spectrosc. Relat. Phenom.*, 1991, **56**, 381–388.
78 S. Bassaki, H. Niazi, F. Golestani-Fard, R. Naghizadeh and R. Bayati, Enhanced Photocatalytic Activity in p-NiO Grafted n-TiO2 Porous Coatings, *J. Mater. Sci. Technol.*, 2015, **31**, 355–360.
79 J. Guo, W. Fu, H. Yang, Q. Yu, W. Zhao, X. Zhou, Y. Sui, J. Ding, Y. Li, S. Cheng and M. Li, A NiO/TiO_2 junction electrode constructed using self-organized TiO_2 nanotube arrays for highly efficient photoelectrocatalytic visible light activations, *J. Phys. D: Appl. Phys.*, 2010, **43**, 245202.
80 P. Parthenidis, K. N. Maroulas, E. Evgenidou, G. Z. Kyzas and D. A. Lambropoulou, Synthesis, characterization and application of GO-ZnO photocatalyst for the enhanced degradation of azole fungicides: Performance, activation of oxidants, transformation products and toxicity, *J. Water Proc. Eng.*, 2025, **74**, 107824.
81 R. Kumar and M. A. Barakat, Flexible multifunctional chitosan/graphene oxide/polyaniline hydrogel thin films for adsorption of ibuprofen from aqueous solution, *Cellulose*, 2024, **31**, 4347–4366.
82 M. A. Suara, S. O. Ganiyu and M. Gamal El-Din, Semiconductor-based solar photocatalytic degradation of surrogate naphthenic acids: Insights on degradation mechanism and the effects of pH, water matrix, and compound structure on the degradation kinetics, *J. Water Proc. Eng.*, 2024, **67**, 106154.
83 Z. Xu, N. Zada, F. Habib, H. Ullah, K. Hussain, N. Ullah, M. Bibi, M. Bibi, H. Ghani, S. Khan, K. Hussain, X. Cai and H. Ullah, Enhanced Photocatalytic Degradation of Malachite Green Dye Using Silver–Manganese Oxide Nanoparticles, *Molecules*, 2023, **28**, 6241.
84 Z. Ur Rahman, U. Shah, A. Alam, Z. Shah, K. Shaheen, S. Bahadar Khan and S. Ali Khan, Photocatalytic degradation of cefixime using CuO-NiO nanocomposite photocatalyst, *Inorg. Chem. Commun.*, 2023, **148**, 110312.
85 P. Gao, Z. Li, L. Feng, Y. Liu, Z. Du and L. Zhang, Construction of novel MWCNTs/Bi_4O5I_2 nanosheets with enhanced adsorption and photocatalytic performance for the degradation of tetracycline: Efficiency, mechanism and regeneration, *Chem. Eng. J.*, 2022, **429**, 132398.
86 B. Akman and O. Aras, Usability, durability and regeneration of Ag/ZnO coated microreactor for photocatalytic degradation of methylene blue, *J. Mol. Struct.*, 2022, **1251**, 132003.
87 L. Xu, L. Qi, Y. Han, W. Lu, J. Han, W. Qiao, X. Mei, Y. Pan, K. Song, C. Ling and L. Gan, Improvement of Fe2+/peroxymonosulfate oxidation of organic pollutants by promoting Fe^{2+} regeneration with visible light driven g-C_3N_4 photocatalysis, *Chem. Eng. J.*, 2022, **430**, 132828.
88 E. M. N. T. Edirisooriya, P. S. Senanayake, P. Xu and H. Wang, Recyclability and regeneration of Au/TiO2 nanocomposite and Pt/TiO2 atom-nano composite

catalysts in photo-reforming plastics for hydrogen production, *J. Environ. Chem. Eng.*, 2025, **13**, 116467.

89 Y. Qiu, J. Yan, X. Liu, Y. Pang, Y. Ding and F. Lyu, A novel g-C3N4-SH@konjac glucomannan composite aerogel for patulin removal from apple juice and its photocatalytic regeneration, *Food Chem.*, 2024, **451**, 139421.

90 H. Kwang Benno Park, P. Kumar, I. Kebaili, I. Boukhris, Y. Hwan Joo, T. Hyun Sung and A. Kumar, Optimization and modelling of magnesium oxide (MgO) photocatalytic degradation of binary dyes using response surface methodology, *Sci. Rep.*, 2024, **14**, 9412.

91 S. Verma, B. Tirumala Rao, R. Singh and R. Kaul, Photocatalytic degradation kinetics of cationic and anionic dyes using Au–ZnO nanorods: Role of pH for selective and simultaneous degradation of binary dye mixtures, *Ceram. Int.*, 2021, **47**, 34751–34764.

92 M. H. Barzegar, M. M. Sabzehmeidani, M. Ghaedi, V. M. Avargani, Z. Moradi, V. A. L. Roy and H. Heidari, S-scheme heterojunction g-C3N4/TiO2 with enhanced photocatalytic activity for degradation of a binary mixture of cationic dyes using solar parabolic trough reactor, *Chem. Eng. Res. Des.*, 2021, **174**, 307–318.

93 K. Vinodgopal and P. V. Kamat, Enhanced Rates of Photocatalytic Degradation of an Azo Dye Using SnO2/TiO2 Coupled Semiconductor Thin Films, *Environ. Sci. Technol.*, 1995, **29**, 841–845.

94 A. Kumar and G. Pandey, Preparation and photocatalytic activity of TiO2/PPy/GO for the degradation of Rose Bengal and Victoria Blue dye in visible light in aqueous solution, *Desalination Water Treat.*, 2018, **114**, 265–284.

95 J. Song, X. Wang, Ou-Po Chen, C.-K. Chen and C.-T. Chang, Photocatalytic Degradation of Reactive Black-5 Dye with Novel Graphene-Titanium Nanotube Composite, *Sep. Sci. Technol.*, 2015, **50**, 1394–1402.

96 A. M. El-Khawaga, H. Tantawy, M. A. Elsayed and A. I. A. A. El-Mageed, Development of novel reduced graphene oxide/metalloporphyrin nanocomposite with photocatalytic and antimicrobial activity for potential wastewater treatment and medical applications, *Sci. Rep.*, 2024, **14**, 27916.

97 O. H. Abuzeyad, A. M. El-Khawaga, H. Tantawy, M. Gobara and M. A. Elsayed, Reduced Graphene Oxide Loaded with ZCF Magnetic Nanoparticles as a Promising Photocatalyst and Antibacterial Agent, *J. Cluster Sci.*, 2024, **36**, 1.

98 D. Singh, K. M. Batoo, S. Hussain, A. Kumar, Q. H. Aziz, F. S. Sheri, H. Tariq and P. Singh, Enhancement of the photocatalytic activity of rGO/NiO/Ag nanocomposite for degradation of methylene blue dye, *RSC Adv.*, 2024, **14**, 2429–2438.

99 R. Xu, G. Wei, Z. Xie, S. Diao, J. Wen, T. Tang, L. Jiang, M. Li and G. Hu, V2C MXene–modified g-C3N4 for enhanced visible-light photocatalytic activity, *J. Alloys Compd.*, 2024, **970**, 172656.